



Pergamon

Available online at www.sciencedirect.com

SCIENCE @ DIRECT®



Acta Materialia 51 (2003) 3333–3349

www.actamat-journals.com

Kinetic modeling of phase transformations occurring in the HAZ of C-Mn steel welds based on direct observations

J.W. Elmer^{a,*}, T.A. Palmer^a, W. Zhang^b, B. Wood^a, T. DebRoy^b

^a Lawrence Livermore National Laboratory, University of California, P.O. Box 808, Livermore, CA 94551, USA

^b The Pennsylvania State University, University Park, PA 16802, USA

Received 18 November 2002; accepted 13 January 2003

Abstract

In situ Spatially Resolved X-Ray Diffraction (SRXRD) experiments were performed in the heat-affected zone (HAZ) of gas tungsten arc (GTA) welds of AISI 1005 C-Mn steel to directly observe welding induced phase transformations. These real-time observations were semi-quantified using diffraction peak profile analysis to construct a phase transformation map revealing ferrite (α) and austenite (γ) phase concentration gradients in the HAZ. Weld thermal cycles were calculated using a three-dimensional heat transfer and fluid flow model and then combined with the SRXRD phase map to provide a complete description of the HAZ under actual welding conditions. Kinetic modelling of the $\alpha \rightarrow \gamma$ phase transformation during heating was performed using a Johnson–Mehl–Avrami analysis, modified to take into account non-uniform weld heating and transformation in the $\alpha + \gamma$ two-phase field. The results provide the most accurate JMA kinetic parameters to date for this alloy, $n=1.45$ and $\ln(k_0)=12.2$, for an activation energy $Q=117.1$ kJ/mole. Using this kinetic description of the $\alpha \rightarrow \gamma$ phase transformation, time temperature transformation (TTT) and continuous heating transformation (CHT) diagrams for this alloy were constructed to illustrate how the combination of SRXRD experiments and numerical modeling from one weld can be used to predict phase transformations for a variety of welding and heat treating applications.

© 2003 Acta Materialia Inc. Published by Elsevier Science Ltd. All rights reserved.

Keywords: Spatially resolved X-ray diffraction; Phase transformations; Kinetics; Welding; Steels

1. Introduction

The investigation of phase transformations in steels is important because of the extensive range of microstructures and the resulting mechanical properties that steels can achieve through different

processing conditions. Transformations between the body centered cubic (bcc) form of iron (α -ferrite) and the face centered cubic (fcc) form of iron (γ -austenite) are principally responsible for the microstructure and properties of steels, and the transformation between the two phases has been studied in great detail for many decades [1–3]. Optimized thermal–mechanical processing treatments for wide varieties of steels have been established [4–6]. However, when steels are welded, the optimized base metal properties are altered by the

* Corresponding author. Tel.: +1-925-422-6543; fax: +1-925-423-7040.

E-mail address: elmer1@llnl.gov (J.W. Elmer).

localized weld thermal cycles. The result is the creation of microstructures in the fusion zone (FZ) and heat affected zone of the welds that are significantly different than those of the base metal, creating non-optimal properties in welded joints [7–10].

In a previous paper SRXRD was used to investigate microstructural evolution in the HAZ of AISI 1005 steel welds by directly identifying and mapping the phases that exist in the HAZ during welding [11]. For this C-Mn steel, regions of annealing, recrystallization, partial transformation and complete transformation to α -Fe, γ -Fe, and δ -Fe phases were identified using SRXRD in a qualitative fashion, however, the results were not quantified at that time. Further analysis of the major Bragg reflections in the SRXRD patterns showed that significant additional information was contained in the data regarding the relative fractions of the α and γ phases present during the transformation. Some of this data was used to provide a semi-quantitative measure of the relative fractions of α and γ present during the $\alpha \rightarrow \gamma$ transformation on heating. From this semi-quantitative SRXRD data, kinetic information about the $\alpha \rightarrow \gamma$ phase transformation on heating was extracted [12,13] using a modified non-isothermal Johnson–Mehl–Avrami (JMA) analysis and the results of a well tested three-dimensional (3D) numerical heat transfer and fluid flow model [14–17].

In this paper, previously published SRXRD results [11] are analyzed to produce the entire semi-quantitative phase map of the $\alpha \rightarrow \gamma \rightarrow \alpha$ phase transformation in the HAZ of AISI 1005 steel. This map represents a considerable amount of effort and reveals for the first time this important phase transformation sequence in steel under the thermal cycles produced during arc welding. Analysis of this data using transport phenomena based numerical modeling determined the kinetics of the phase transformations under various thermal cycles, which can be used to predict $\alpha \rightarrow \gamma$ phase transformations under a wider range of welding conditions than can be studied by SRXRD alone.

2. Experimental procedures

2.1. SRXRD experiments

Gas tungsten arc (GTA) welds have been made on AISI 1005 steel (0.05 C, 0.31 Mn, 0.18 Si, 0.11 Ni, 0.10 Cr, 0.009 P, 0.008 Cu, 0.005 S, <0.005 Al, <0.005 Nb, <0.005 Mo, <0.005 Ti, <0.005 V; by wt. percent) cylindrical forged bar samples. These samples were machined from 10.8 cm diameter forged bar stock into welding samples, 12.7 cm long and 10.2 cm diameter. Circumferential welds were then made on the cylindrical steel bars in an environmentally sealed chamber to avoid atmospheric contamination of the weld. A brief summary of the welding parameters used here is given in Table 1. Further details of the welding experiments have been previously reported [11].

The in situ SRXRD experiments reported here were performed during welding using the 31-pole wiggler beam line, BL 10-2 [18] at SSRL with SPEAR (Stanford Positron-Electron Accumulation Ring) operating at an electron energy of 3.0 GeV and an injection current of ~100 mA. In these experiments a focused monochromatic synchrotron X-ray beam is passed through a 260 μ m tungsten pinhole to render a sub-millimeter beam on the sample at an incident angle of ~25°. This setup yields a beam flux on the sample of ~10¹⁰ photons/s, which was determined experimentally using an ion chamber immediately downstream from the pinhole. A photon energy of 12.0 keV ($\lambda = 0.1033$ nm) was chosen to facilitate phase

Table 1
Summary of GTA welding parameters used in the SRXRD experiments

Welding electrode	W-2% Th
Electrode diameter (mm)	4.7
Torch polarity	DCEN
Maximum current (A)	130
Background current (A)	90
Weld voltage (V)	17.5
Pulsing frequency (Hz)	300
Peak on time (%)	50
Shielding gas	Helium
Travel speed (mm/sec)	0.6
Resulting fusion zone width (mm)	~9

identification and to be far enough in energy above the Fe K-edge (7.112 keV) to minimize the background contribution due to Fe K-fluorescence from the steel sample [23].

X-ray diffraction patterns at each location were recorded using a 50 mm long 2048 element position sensitive Si photodiode array detector. The array was mounted on a dual-stage water cooled Peltier effect thermoelectric cooler at a distance of approximately 10 cm behind the weld to cover a 2θ range from 25–55°. This 2θ range was optimized to contain a total of six diffraction peaks, three from the bcc phases (α -Fe or δ -Fe) and three from the fcc phase (γ -Fe). During a typical SRXRD run, 40 diffraction patterns were gathered at intervals of 250 μm along a pre-determined path, spanning a range of 10 mm through the HAZ. The accuracy of the positioning of the SRXRD beam with respect to the fusion boundary for a given weld is ± 0.5 mm. This estimate considers the initial positioning the X-ray beam, and dynamic fluctuations in the fusion boundary as discussed elsewhere for these 1005 steel welds [11]. Additional details of the SRXRD experiments are published elsewhere [19–22].

2.2. Diffraction pattern profile analysis

Analysis of each peak in each diffraction pattern was performed to determine the semi-quantitative volume fractions of ferrite and austenite present at each SRXRD location. This analysis measured the integrated intensity of each peak in each diffraction pattern using a sum of one or more Gaussian peak profile fitting functions [21,24]. The area and FWHM values of the fitted peaks were then determined using an automated curve-fitting routine developed in Igor Pro®, Version 4.0 [25].

The raw integrated intensities of the diffraction peaks were then converted into relative phase intensities. This conversion is based on the effects of a number of factors on the resulting intensity of a given peak. In this method, the peak area or integrated intensity of each peak is measured and then converted to relative fraction of each phase by considering the crystal structure, the Lorentz polarization factor, and the temperature. The overall methodology used is described in Appendix A.

It should be noted that the conversion of the integrated intensities to a volume fraction is not calibrated against a known metallographic standard, since the room temperature microstructure of the 1005 steel does not contain any austenite.

3. Results

3.1. Phase equilibria and thermal modeling

The phase transformation sequence in the 1005 steel was calculated from thermodynamic relationships using ThermoCalc [26]. These calculations were used to determine the transformation temperatures for the AISI 1005 steel used in this investigation by considering the effects of Fe, C, Si, Mn, Ni and Cr on the liquid, ferrite, austenite, and cementite phase fields. The phase-boundary temperatures, as calculated by ThermoCalc for this multi-component alloy, are illustrated as a pseudobinary diagram in Fig. 1. As a verification of these calculations, dilatometry was also performed on a base metal sample to directly measure the A1 and A3 temperatures, which are both critical to the resulting phase transformations that occur during welding. Specimens measuring 50 mm long and 3

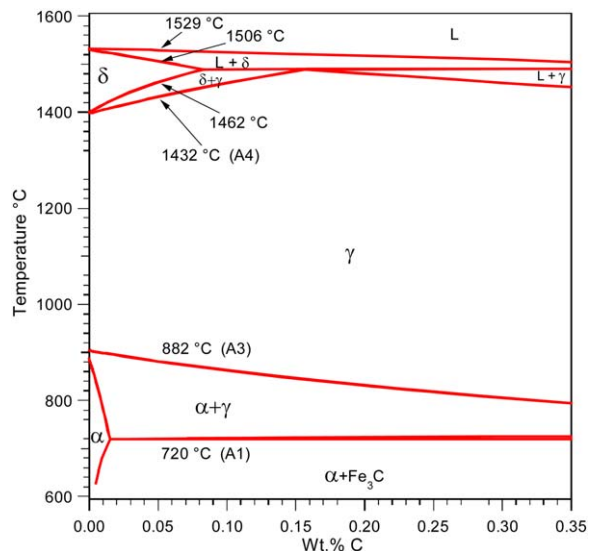


Fig. 1. Calculated pseudobinary Fe-C phase diagram for the AISI 1005 steel.

mm in diameter were heated at a rate of 3 °C/min in a conventional horizontal tube type dilatometer to a peak temperature of 1500 °C. The results confirmed the calculated A1 temperature, but the measured A3 temperature was 931 °C, which is higher than the calculated value. It is this dilatometric value for the A3 temperature which is used for calculating the kinetics of the $\alpha \rightarrow \gamma$ phase transformation.

Weld thermal cycles were calculated using an extensively tested 3D numerical heat transfer and fluid flow model [12,13]. In this model, the transient nature of the problem is transformed into a steady-state one by using a coordinate system moving with the heat source [14,15]. The equations of conservation of mass, momentum and energy in three-dimensional form were discretized using the power law scheme and numerically solved by the SIMPLER algorithm [27]. A $77 \times 40 \times 49$ grid system was used in the calculation, and the corresponding computational domain had dimensions of 163 mm in length, 60 mm in width, and 42 mm in depth.

After obtaining the steady-state temperature field, the thermal cycle at any given location (x,y,z) was calculated using the following equation:

$$T(x,y,z,t_2) = \frac{T_s(\zeta_2,y,z) - T_s(\zeta_1,y,z)}{\zeta_2 - \zeta_1} V_s(t_2 - t_1) + T(x,y,z,t_1) \quad (1)$$

where $T(x,y,z,t_2)$ and $T(x,y,z,t_1)$ are the temperatures at times t_2 and t_1 , respectively, $T_s(\zeta_2,y,z)$ and $T_s(\zeta_1,y,z)$ are the steady-state temperatures at coordinates (ζ_2,y,z) and (ζ_1,y,z) , respectively, V_s is the welding speed and $(\zeta_2 - \zeta_1)$ is the length welded in time $(t_2 - t_1)$.

The calculated thermal profiles for the GTA weld are shown in Fig. 2(a)–(c). Fig. 2(a) shows plots of the calculated temperature profiles parallel to the welding direction at the top surface for locations starting at the weld centerline and moving outward to a distance of 10 mm. The peak temperature in the weld pool is 1763 °C, and then drops to the solidus (1506 °C) at the fusion boundary ($Y = 4.4$ mm), then continues to decrease to the A1 temperature (720 °C) at the $Y = 7.7$ mm position. This region of the weld roughly defines

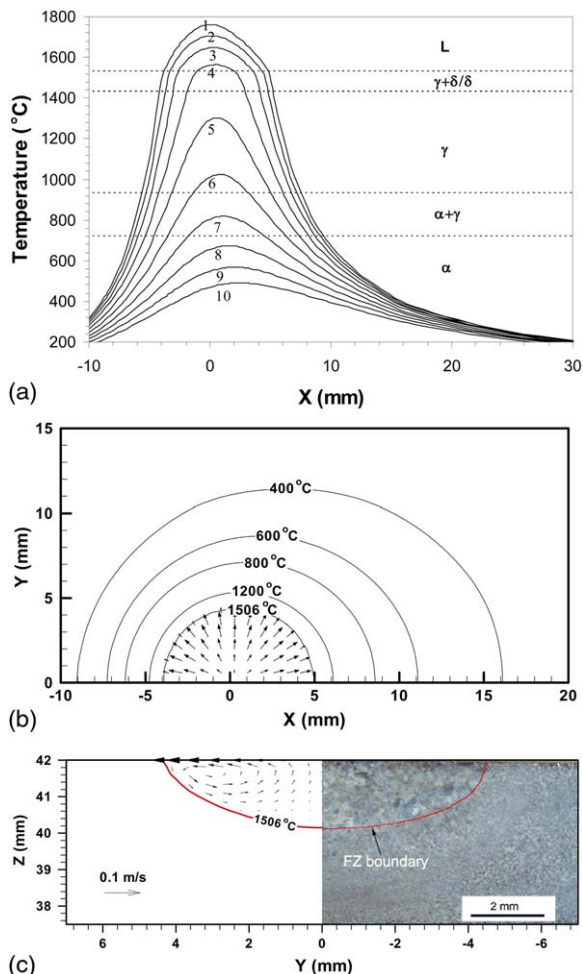


Fig. 2. (a) Temperature versus distance plot showing temperature cycles parallel to the welding direction at various distances from the weld center line. 1: 0 mm; 2: 2 mm; 3: 3 mm; 4: 4 mm; 5: 5 mm; 6: 6 mm; 7: 7 mm; 8: 8 mm; 9: 9 mm; 10: 10 mm. (b) Contour plot of the calculated temperature field assuming mirror symmetry about the x -axis. The heat source is centered at $(0,0)$ and the material is moving from left to right below the stationary arc. (c) Comparison between the calculated (at location $x = 0$) and experimental fusion zone geometry at the transverse plane. The superimposed fusion zone boundary was measured on the welded sample.

the HAZ, which spans to a distance of approximately 2.3 mm. Fig. 2(b) shows a contour plot, in which mirror symmetry is assumed about the x -axis, of the temperature fields in the HAZ. Fig. 2(c) compares the calculated fusion zone boundary represented by the solidus temperature of 1506 °C

with that determined metallographically, showing good agreement between the two.

3.2. Base metal and HAZ microstructures

The HAZ microstructure in the 1005 steel weld was revealed by lightly polishing the weldment surface and etching in a 2% nital (nitric acid and alcohol) solution [11]. Fig. 3(a) shows the base metal microstructure, which is largely composed of equiaxed ferrite grains having an average diameter of 21.6 μm . Small regions of pearlite are present in the base metal microstructure at grain boundary edges and corners. Fig. 3(b) shows the microstructure of the partially transformed region at a location 2.5 mm from the fusion line. Isolated clusters of grains with diameters much smaller than that of the base metal are present at some of the ferrite grain boundary edges and corners. These clusters result from the transformation of cement-

ite, which is contained within the pearlite, to a mixture of α -Fe and γ -Fe on heating. Numerous etching pits are also observed uniformly throughout the microstructure, which are most likely the result of small carbide and or nitride particles that have formed during the heating cycle of the weld [28].

Fig. 3(c) shows a typical microstructure from the fine-grained region of the HAZ at a location 1.25 mm from the fusion line. The grains are equiaxed and have an average diameter of 10.5 μm . This smaller grain size results from the α -Fe to γ -Fe transformation, during which the new γ -Fe grains nucleate at numerous locations within the α -Fe grains and produce a finer grain size. As welding proceeds, these new γ -Fe grains in the fine-grained region of the HAZ grow. The amount of grain growth increases rapidly as the weld fusion zone is approached, leading to the formation of the coarse grained microstructural region of the HAZ as shown in Fig. 3(d) at a location 0.25 mm from the

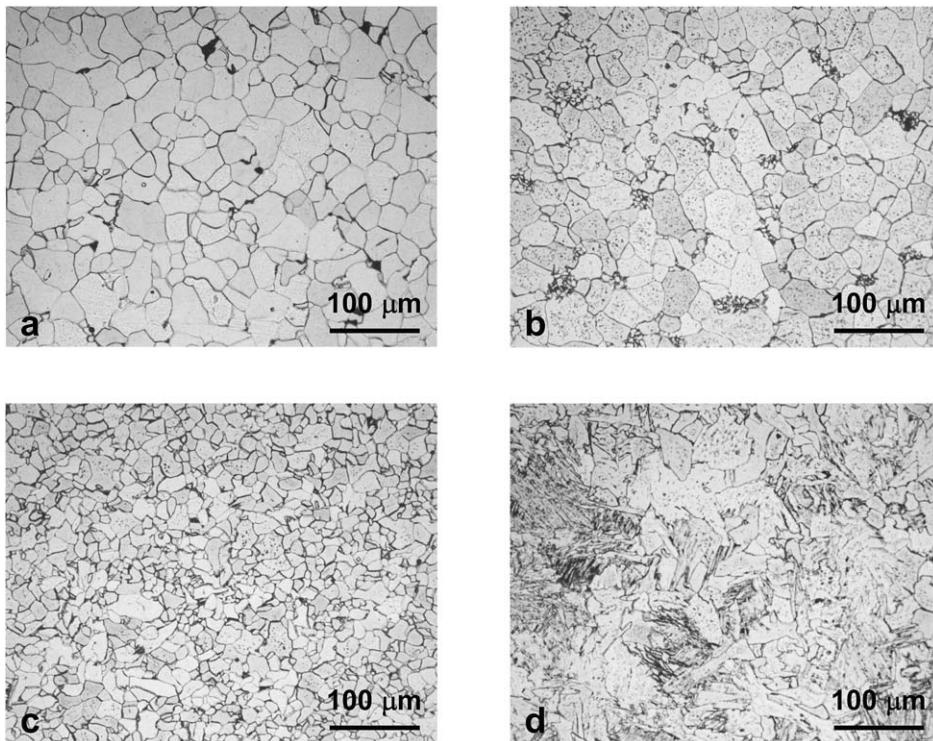


Fig. 3. Optical micrographs of the AISI 1005 steel fusion weld at various locations in the HAZ: (a) base metal, (b) partially transformed region at 2.5 mm from the fusion line, (c) fine grained region 1.25 mm from the fusion line, and (d) coarse grained region 0.25 mm from the fusion line.

fusion line. This microstructure contains primarily α -Fe grains (at room temperature) that have transformed from the large prior γ -Fe grains.

3.3. SRXRD semi-quantitative phase map

The SRXRD experimental data were first used to identify the spatial distribution of the α -Fe, γ -Fe, and δ -Fe phases in the HAZ [11]. Each SRXRD diffraction pattern was further analyzed to determine the relative fractions of α and γ at each discrete location in the HAZ. Table 2 summarizes the relative austenite fractions on the front (heating) side of the weld starting at positions close to the weld centerline ($Y=0$) and moving outward into the HAZ to a position near the base metal at $Y = 8.75$ mm. Nine different paths are indicated, starting ahead of the weld where no transformation to austenite was observed ($X = -6$ mm), and moving back to the $X = 1$ mm position, where the maximum transformation to austenite had occurred. The temperatures are highest near the weld centerline, and the transformation to austenite at these locations is either complete or nearly so.

As the beam moves further from the weld centerline (increasing Y) for a given SRXRD path, ferrite begins to co-exist with austenite in increasing proportions. The α/γ co-existence region typically extends five or six SRXRD steps (0.25 mm per step), after which only the ferrite phase remains. This trend repeats for different x -locations. However, the point where the co-existence starts and ends continues to move outward from the weld centerline. At the $X = 1$ mm location, the single-phase austenite field reaches its furthest distance from the centerline of the weld, corresponding to the region of greatest heating.

Table 3 summarizes the results on the back (cooling) side of the weld. In this table, the austenite fraction is again given at each SRXRD location starting close to the weld centerline ($Y = 0$) and moving outward to a position of $Y = 8.75$ mm. Eleven additional SRXRD paths are listed, starting at the $X = 2$ mm position and moving back to the $X = 11$ mm position. The region of co-existence between austenite and ferrite now begins to return towards the centerline of the weld as the transformation from austenite to ferrite occurs during cool-

ing. At the $X = 7$ mm location, the α/γ co-existence region reaches the HAZ/FZ boundary ($Y \sim 4.25$ mm). At this point, the hottest portion of the HAZ, where the single-phase austenite region spans the greatest distance, begins to transform to ferrite. For all locations further behind the weld, the amount of austenite decreases until only small amounts of austenite remain at the $X = 11$ mm location.

Based on these measurements, a phase map was developed to show the changes occurring in the austenite volume fraction during heating and cooling. A semi-quantitative map of the austenite volume fractions in the weld HAZ is shown in Fig. 4, superimposed on several calculated weld isotherms of interest. Unlike the previous qualitative phase field map [11], this map provides specific information concerning the effects of the welding process on the ferrite/austenite phase balance in the regions surrounding the weld pool. In this plot, the shading indicates the fraction austenite, which varies from 0% austenite (blue) to 100% austenite (red). In a few locations the transformation to the high temperature bcc phase (δ -Fe) was observed adjacent to the weld pool (blue shading). The individual SRXRD line scans were made perpendicular to the welding direction, and show a variation in austenite fraction from 0–1 over a region approximately 1.5 mm wide.

These data were first used to calculate lines of constant transformation to the austenite phase using regression analysis. To do this, each set of SRXRD data for a constant X value was best fit using a four parameter sigmoidal distribution given in Eq. (2).

$$y = y_0 + a / (1 + \exp(-(x-x_0)/b)), \quad (2)$$

where y is the austenite fraction, x_0 , y_0 , a , and b are four parameters that control the shape of the sigmoidal curve, and x is the distance from the weld centerline.

Here the sigmoidal distribution is used only as a means to fit the SRXRD data to calculate the Y -axis location for transformation to 5%, 50%, and 95% austenite. The results are plotted in Fig. 5(a) for one SRXRD pass, showing the sigmoidal fit to the experimental data at the $X = -3.5$ mm position. In this plot the individual measured values for the

Table 2

Semi-quantitative analysis results showing the fraction austenite at each of the SRXRD locations on the heating side of the weld. The coordinates are for the X-ray beam which is measured with respect to the center of the weld ($X = 0$, $Y = 0$). Here, the coordinate X refers to the distance ahead of (negative values) or behind (positive values) the center of the weld parallel to the welding direction, while Y corresponds to the distance from the centerline of the weld perpendicular to the welding direction

Y (mm)	X (mm)								
	-6	-5	-4	-3.5	-3	-2.5	-2	0	1
1	0	0.581	1	1	–				
1.25	0	0.691	1	1	–				
1.5	0	0.523	1	1	–	–			
1.75	0	0.475	0.880	1	–	–			
2	0	0.458	0.786	1	–	–	–		
2.25	0	0.284	0.665	1	–	–	–		
2.5	0	0.302	0.795	1	1	–	–	–	–
2.75	0	0.149	0.476	1	1	1	–	–	–
3	0	0.085	0.294	1	1	1	–	–	–
3.25	0	0.050	0.062	1	1	1	1	–	–
3.5	0	0.020	0.029	0.989	1	1	1	–	–
3.75	0	0.003	0.002	0.939	1	1	1	–	–
4	0	0	0	0.778	1	1	1	–	–
4.25	0	0	0	0.480	1	1	1	1	–
4.5	0	0	0	0.287	1	1	1	1	–
4.75	0	0	0	0.103	1	1	1	1	1
5	0	0	0	0.040	0.705	1	1	1	1
5.25	0	0	0	0.014	0.187	0.873	1	1	1
5.5	0	0	0	0	0.094	0.707	1	1	1
5.75	0	0	0	0	0.012	0.241	0.921	1	1
6	0	0	0	0	0	0.103	0.558	1	1
6.25	0	0	0	0	0	0.038	0.224	1	1
6.5	0	0	0	0	0	0.005	0.102	0.821	1
6.75	0	0	0	0	0	0	0.033	0.331	1
7	0	0	0	0	0	0	0	0.198	0.708
7.25	0	0	0	0	0	0	0	0.070	0.244
7.5	0	0	0	0	0	0	0	0.011	0.073
7.75	0	0	0	0	0	0	0	0.003	0.048
8	0	0	0	0	0	0	0	0	0.012
8.25	0	0	0	0	0	0	0	0	0
8.5	0	0	0	0	0	0	0	0	0
8.75	0	0	0	0	0	0	0	0	0

austenite fraction are plotted along with the best-fit curve, showing good correlation between the two.

After fitting the data for each of the SRXRD runs, lines of constant transformation to austenite were constructed around the weld pool. These data are plotted in Fig. 5(b), along with the calculated isotherms superimposed on the SRXRD data. The isotherms show the relationship between the fraction transformed and the phase regions predicted by the phase diagram and the modeled weld tem-

peratures. The lines of constant transformation follow approximately the same general trend as the isotherms, which rise steeply just ahead of the weld pool, where the temperature gradients are the largest, and curve back behind the weld pool. There is some scatter in the experimental data, as expected, based on the accuracy of positioning the SRXRD beam and variations in weld pool width from run to run.

This data can further be represented in time–

Table 3

Semi-quantitative analysis results showing the fraction austenite at each of the SRXRD locations on the cooling side of the weld. As in Table 2, the coordinates are for the X-ray beam which is positioned with respect to the center of the weld ($X = 0$, $Y = 0$). The coordinate X refers to the distance behind the center of the weld parallel to the welding direction, while Y corresponds to the distance from the centerline of the weld perpendicular to the welding direction

Y (mm)	X (mm)											
	2	3	4	4.5	5	6	7	8	9	10	11	
1			–	–		–						
1.25			1	–	1	1						
1.5			1	–	1	–						
1.75			–	–	–	1						
2		–	1	–	–	1						
2.25		–	1	–	1	–						
2.5	–	–	–	–	–	1						
2.75	–	–	1	1	–	–						
3	–	–	1	1	1	1						
3.25	–	–	–	–	–	–						
3.5	–	1	–	1	–	–						
3.75	–	–	–	–	–	–						
4	–	1	1	–	–	1						
4.25	–	–	–	–	1	1	0.756	–	0.096	0.191	0.260	
4.5	–	–	1	–	1	1	0.900	0.200	0.205	0.013	0.100	
4.75	1	1	1	–	1	1	0.139	0.320	0.187	–	0.049	
5	–	1	1	1	1	1	0.289	0.340	0.036	0.009	0.005	
5.25	1	1	1	1	1	1	0.664	0.397	0.086	0.157	0.083	
5.5	1	1	1	0.957	0.819	0.899	0.422	0.492	0.105	0.184	0.283	
5.75	1	1	1	0.945	0.696	0.749	0.175	0.285	0.043	0.091	0.111	
6	1	1	1	0.592	0.457	0.320	0.114	0.322	0.088	0.020	0.150	
6.25	1	1	0.943	0.242	0.249	0.259	0.058	0.143	0.003	0	0.017	
6.5	1	1	0.676	0.173	0.187	0.157	0.011	0.090	0	0	0	
6.75	1	1	0.387	0.089	0.055	0.095	0.004	0.061	0	0	0	
7	0.964	0.996	0.222	0.036	0.046	0.027	0.003	0.034	0	0	0	
7.25	0.708	0.609	0.094	0.017	0.008	0.011	0	0	0	0	0	
7.5	0.473	0.404	0.048	0.010	0	0	0	0	0	0	0	
7.75	0.204	0.178	0.031	0	0	0	0	0	0	0	0	
8	0.055	0.067	0.003	0	0	0	0	0	0	0	0	
8.25	0.016	0.009	0	0	0	0	0	0	0	0	0	
8.5	0	0	0	0	0	0	0	0	0	0	0	
8.75	0	0	0	0	0	0	0	0	0	0	0	

temperature-transformation space. Numerous HAZ temperature profiles taken parallel to the welding direction are superimposed onto a single plot, and the iso-fraction lines as determined from the SRXRD data are then plotted on the respective calculated temperature profiles. Fig. 6 shows this plot with the calculated A1 and A3 temperatures, which indicate the phase transformation start and finish locations under equilibrium conditions. In this fig-

ure, the temperature profile with the highest peak temperature corresponds to a location $Y = 2.94$ mm from the centerline of the weld and the temperature profile with the lowest peak temperature corresponds to $Y = 7.7$ mm from the centerline of the weld. As indicated in the figure, significant superheat is required to initiate the transformation and to complete the $\alpha \rightarrow \gamma$ transformation.

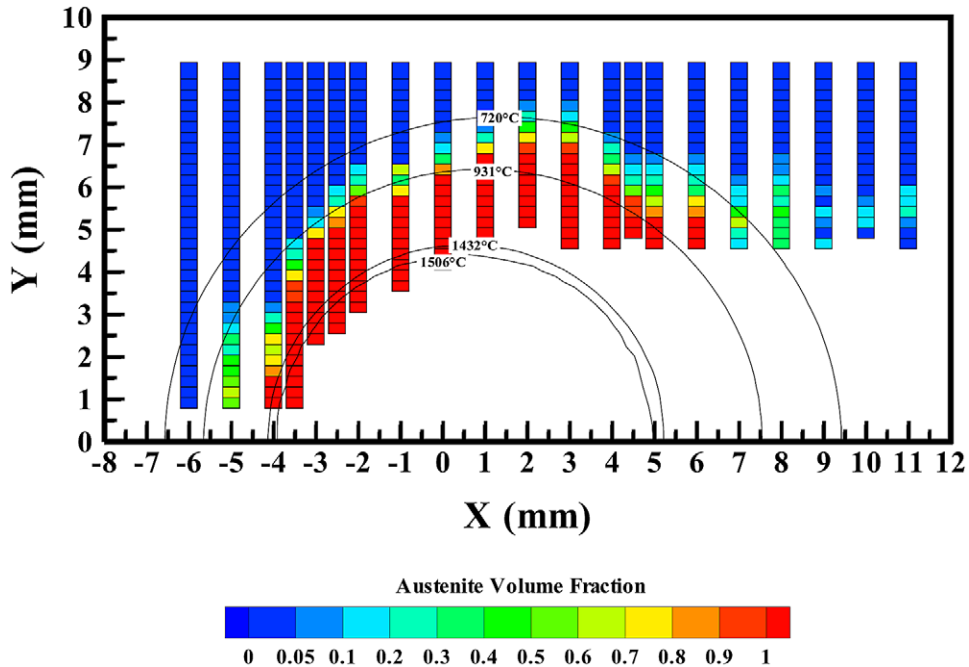


Fig. 4. SRXRD Semi-quantitative phase map plotting the volume fraction austenite in the region undergoing the α - γ phase transformation. The calculated isotherms superimposed on the map correspond to the liquidus (1529 °C), the γ solidus (A4) (1432 °C), the $\alpha + \gamma$ solidus (A3) (931 °C), and the eutectoid temperature (A1) (720 °C).

4. Discussion

4.1. Kinetics of $\alpha \rightarrow \gamma$ transformation on heating

The SRXRD data mapped in Fig. 4 contain important kinetic information about the phase transformations that occur on heating and cooling during the welding of a 1005 steel. However, in order to extract kinetic information for the ferrite/austenite transformation from this map, it is necessary to analyze the results using the calculated weld thermal profiles and a suitable phase transformation model. Here, we use the JMA relationship to analyze the SRXRD results. This model is applicable to phase transformations that involve nucleation and growth and has proven to be useful in the past for developing predictive relationships for the $\alpha \rightarrow \gamma$ phase transformation in this steel [12,13].

The calculated isotherms and velocity fields superimposed on the SRXRD phase map in Fig. 2(b) are replotted in Fig. 7, showing only the details of the $\alpha \rightarrow \gamma$ transformation on the heating

side of the weld. In this figure, the stationary welding electrode is positioned at $X = Y = 0$, and the welded sample moves from right to left along the x direction. The weld pool boundary is represented by the solidus isotherm (1506 °C) of the 1005 steel, while the A1 (720 °C) and A3 (931 °C) temperatures are shown to identify the equilibrium start and finish locations for the $\alpha \rightarrow \gamma$ transformation.

The thermal profiles corresponding to the heating side of the weld, calculated parallel to the welding direction, are further plotted in Fig. 8 at different HAZ locations from $Y = 5.75$ mm to $Y = 6.75$ mm. In this plot, the position parallel to the welding direction was converted from spatial coordinates to temporal coordinates. This transformation was performed by dividing the x -axis spatial coordinate by the welding speed. Here, the X -axis time equal to zero corresponds to the heat source location identified in Fig. 7 as $X = 0$. The peak temperature and heating rates at various locations are plotted in Fig. 8, showing that both parameters decrease with increasing distance from the weld centerline. This variation in peak temperature and

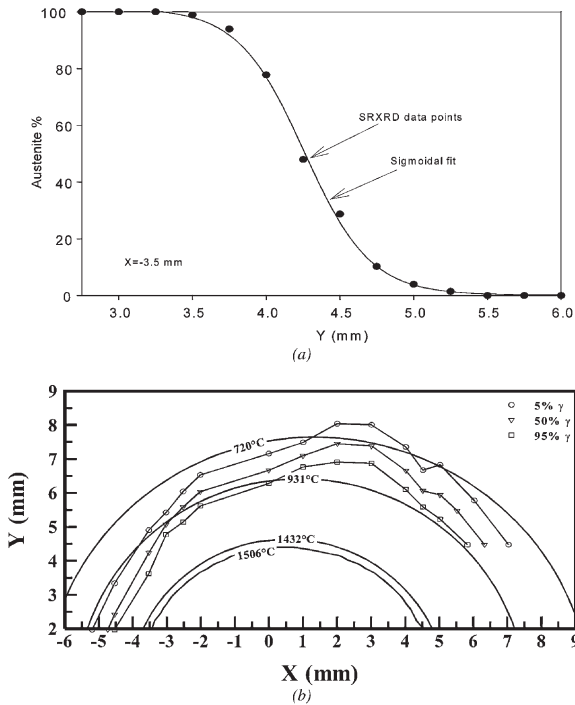


Fig. 5. (a) SRXRD data points, superimposed on the 4-parameter sigmoidal best fit curve, showing the fraction austenite along the $X = -3.5$ mm line. (b) Three iso-transformation lines in the $\alpha + \gamma$ region of the weld HAZ, corresponding to 5%, 50%, and 95% transformation to austenite.

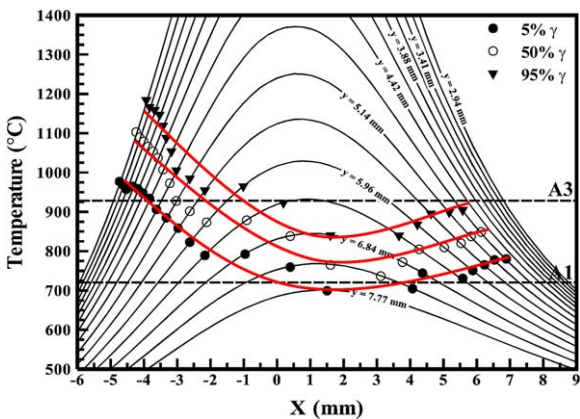


Fig. 6. Isocomposition lines superimposed on the thermal profiles and compared to the A1 and A3 temperatures for 1005 steel.

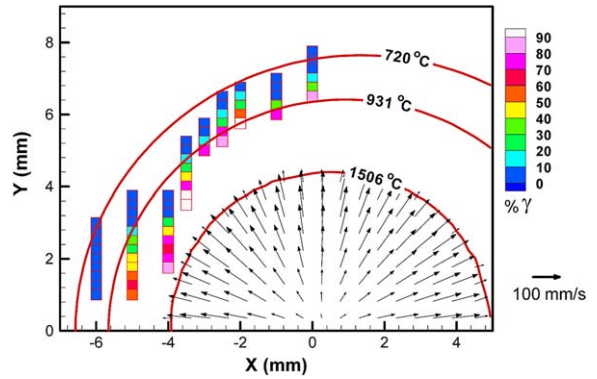


Fig. 7. Spatial distribution of α and γ phases during heating.

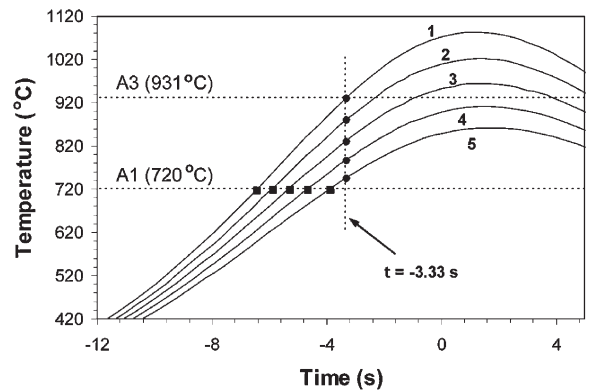


Fig. 8. Calculated thermal cycles at different y locations along $x = -2.0$ mm path. 1: $y = 5.75$ mm; 2: $y = 6.0$ mm; 3: $y = 6.25$ mm; 4: $y = 6.5$ mm; and 5: $y = 6.75$ mm. Time equal to zero was arbitrarily selected to correspond to the heat source location at $x = 0$ in Fig. 7.

heating rates is responsible for the spatial variation of austenite in the HAZ.

In order to illustrate how the temperature profiles influence HAZ phase transformations, the thermal cycles that contribute to the $\alpha \rightarrow \gamma$ transformation for different y -axis locations along the $X = -2$ mm ($t = -3.33$ s) SRXRD path are shown in Fig. 8. The portion of the thermal cycle responsible for the transformation up to these points are indicated by the lines between the solid squares at the transformation start temperature (A1), and the circles which correspond to the location where the SRXRD data was taken. These five paths lead to the variation in fraction austenite from 3.3% (profile 5) to 92.1% (profile 1).

The calculated thermal profiles, as illustrated in Fig. 8, represent the type of data that will be used in conjunction with the additional SRXRD data to develop the kinetic parameters for the $\alpha \rightarrow \gamma$ transformation in the HAZ of this weld. In order to do this, the mechanism for the transformation must be known. Previous work has shown that the $\alpha \rightarrow \gamma$ transformation occurs by the diffusion of carbon, and that under most conditions the reaction rate is controlled by the diffusion of carbon in the austenite phase [29]. The apparent activation energy for this transformation is 117.1 kJ/mole [30], which incorporates both the effects of nucleation and growth on the transformation kinetics. This apparent activation energy is lower than the activation energy for the diffusion of carbon in austenite alone, which is reported to be 135 kJ/mole [31].

In order to model the phase transformation kinetics, the JMA approach will be used to describe the overall transformation rate. This approach can be represented by the following expression [32]:

$$f_c(t) = 1 - \exp\{-(kt)^n\} \quad (3)$$

where $f_c(t)$ is the extent of the transformation at a given time t , n is the JMA exponent, and k is a rate constant given as:

$$k = k_0 \exp\left(-\frac{Q}{RT}\right) \quad (4)$$

where k_0 is a pre-exponential constant, Q is the activation energy of the transformation including the driving forces for both nucleation and growth, R is the gas constant and T is the absolute temperature in K .

Eq. (3) is further modified in Appendix B to derive the JMA-based expression applicable to non-isothermal phase transformations occurring in the $\alpha + \gamma$ two phase region of the HAZ. This modeling approach was combined with the calculated thermal profiles and the SRXRD experimental data to determine the JMA parameters n and k_0 for the given value of Q using a numerical fitting routine applied to the SRXRD data in Table 2 and the computed thermal cycles.

Fig. 9 shows the results of the fitting calculations by comparing the plot of the error between the calculated and experimental γ fraction as a function of $\ln(k_0)$ and n . As shown in this figure, the opti-

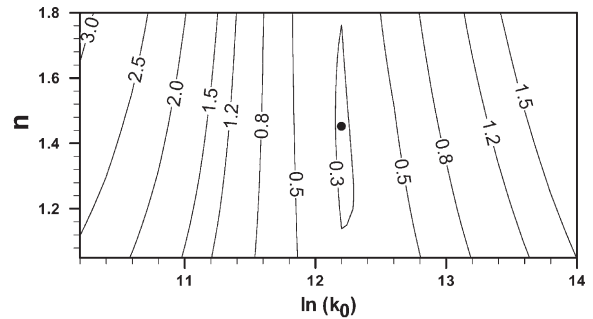


Fig. 9. Calculation of the optimal values of n and k_0 for a Q value of 117.1 kJ/mol. The error field is represented by the contour lines. The minimum error is indicated by the solid dot.

mal JMA parameters for the Q value of 117.1 kJ/mol correspond to the minimum error on this plot and were found to be $\ln(k_0) = 12.3$ and $n = 0.63$. It should be recognized that the activation energy for nucleation and growth used in the fitting program is associated with $\alpha \rightarrow \gamma$ transformation in steels with similar compositions.

Knowing these JMA kinetic parameters it is now possible to calculate the $\alpha \rightarrow \gamma$ phase transformation rates throughout the HAZ where different heating rates and peak temperatures are observed. It is also possible to calculate the boundary in the HAZ where the $\alpha \rightarrow \gamma$ transformation goes to completion, thus marking the front side of the single phase austenite phase field of the HAZ. Furthermore, the kinetic parameters allow us to predict the extent of the $\alpha \rightarrow \gamma$ transformation for any weld heating cycle.

The internal consistency of these kinetic parameters was checked by comparing the austenite fraction at the different SRXRD locations presented in Table 2 to the values calculated using the non-isothermal kinetic Eq. (B8). Fig. 10 compares the results from seven different SRXRD locations, denoted in the plot as symbols, with the calculated values, shown as the solid lines. The overall agreement between the experimentally measured data and the calculated data is reasonable, especially when considering the wide range of heating rates experienced at these different HAZ locations.

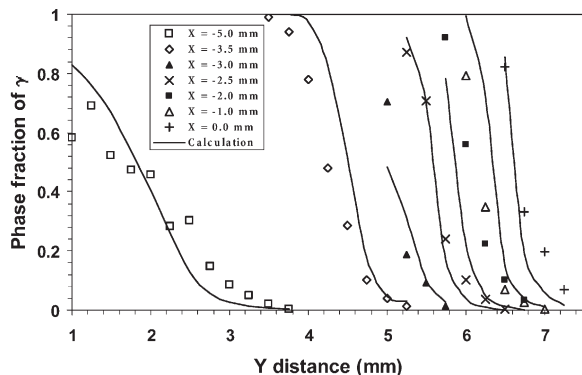


Fig. 10. Comparison between the calculated and SRXRD experimental phase fractions of γ at different monitoring locations.

4.2. TTT and CHT diagrams for 1005 steel welds during heating

There are two main types of transformation diagrams that are useful in understanding transformation kinetics during welding: Continuous Heating Transformation (CHT) and Continuous Cooling Transformation (CCT) diagrams. The first type of diagram can be used to predict the transformations that occur on the heating side of the weld and the latter on the cooling side of the weld. Both types of diagrams can be related to the Time Temperature Transformation (TTT) diagrams that are used to measure the rate of the transformation at a constant temperature.

Using the kinetic parameters from the preceding section, TTT and CHT diagrams were constructed for the $\alpha \rightarrow \gamma$ transformation in the 1005 steel, while the CCT diagram determination will be reserved for future work. The following JMA-based kinetic equation (see Appendix B) and various time-temperature profiles were used in this analysis:

$$\frac{f(t_i)}{F_i} = 1 - \exp\left\{-\left[k_0 \times \exp\left(-\frac{Q}{RT_i}\right) \times (\Delta t + \tau_i)^n\right]\right\} \quad (5)$$

For a TTT diagram, the isothermal relationships can be expressed as a function of the temperature above the A1 temperature as follows:

$$T(t) = T_H \quad (6)$$

where T is the temperature at a given time t , and T_H is the constant transformation temperature.

Incorporating Eq. (6) into Eq. (5), the austenite fraction can be given versus time at the given temperature. The results were then used to construct the TTT diagram shown in Fig. 11 for the 1005 steel. In this plot, the constant transformation lines are compared to the A1 and A3 temperatures for this steel. As shown in this figure, the $\alpha \rightarrow \gamma$ transformation kinetics accelerate rapidly as the temperature increases. The fast rate results from the increase in both the driving force and the diffusivity of carbon in austenite with temperature. Moreover, the transformation can go to completion only at a temperature higher than the A3 temperature (931 °C). The calculated TTT diagram also indicates that for the isothermal formation of austenite, the transformation start time is usually less than 1 s, while the time for completion is less than 10 s.

The CHT diagram was constructed in a similar way as the TTT diagram, but using a constant heating rate as given in equation below:

$$T(t) = T_{A1} + H_T \times t \quad (7)$$

where T_{A1} is the A1 temperature (720 °C) and H_T is the heating rate. The non-isothermal transformation kinetics at various heating rates were then calculated using Eq. (5), and the resulting austenite fraction versus time data were then used to construct the CHT diagram in Fig. 12. The austenite transformation lines are again compared to the A1 and A3 temperatures for the 1005 steel. As shown

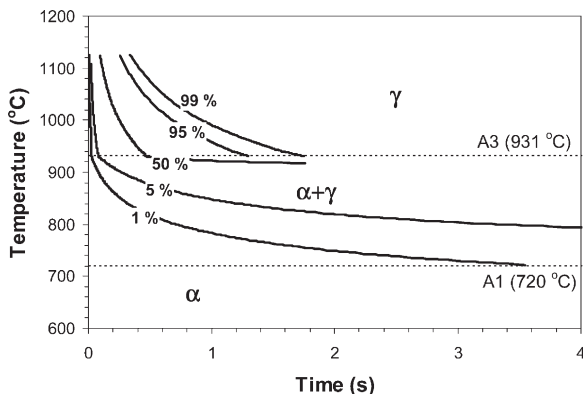


Fig. 11. Calculated TTT diagram for $\alpha \rightarrow \gamma$ transformation during heating of 1005 steel.

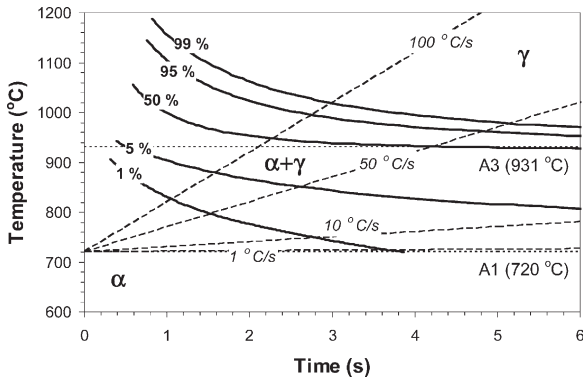


Fig. 12. Calculated CHT diagram for $\alpha \rightarrow \gamma$ transformation during heating of 1005 steel.

in this figure, the transformation rate accelerates rapidly with temperature, and both the start and finish temperatures of the transformation increase with increasing heating rate.

A comparison between Figs. 11 and 12 shows that the time required for an equivalent amount of austenite transformation is longer under the CHT conditions than the TTT conditions. The reason for this behavior is that the total kinetic strength of the transformation is less for the CHT case than for the TTT case, since the time temperature curves are integrated up to the final temperature where the transformation is predicted in the CHT conditions. The CHT diagram for the 1005 steel indicates that for the isothermal formation of austenite, the transformation start time is usually greater than 1 s, while the time for completion is greater than 10 s. In addition, it is apparent that some amount of super heating is required to start and complete the phase transformation to austenite under non-isothermal conditions. For example, using a heating rate of 50 °C/s, Fig. 12 predicts the transformation start (1% austenite) to be 45 °C above the A1 temperature, while the transformation finish (99% austenite) is 135 °C above the A3 temperature.

Thus, using a combination of numerical weld modeling to predict the weld temperature profiles, the SRXRD experimental data, and the JMA phase transformation formalism, a CHT diagram has been constructed for 1005 steel welds. This diagram allows the kinetics of the $\alpha \rightarrow \gamma$ transformation to be calculated over a relatively wide range of HAZ weld heating rates. It should be noted that

the kinetic parameters (k_0 and n) calculated using the SRXRD data, and thus the CHT diagram, depend on the initial microstructure of the base metal.

5. Conclusions

SRXRD phase mapping, numerical temperature modeling, and JMA kinetic calculations were performed to study the kinetics of the $\alpha \rightarrow \gamma$ phase transformation in an AISI 1005 C-Mn steel. This combination of experimental and modeling methods provides previously unavailable insight into this important phase transformation in the HAZ of C-Mn steels. Based on these results, a number of specific conclusions can be made.

1. Diffraction peak analysis of the SRXRD data was used to produce a semi-quantitative map of the phase transformations occurring in the weld HAZ. This work marks the first time that phase transformations have been mapped in the HAZ of a C-Mn steel weld. This data contains all the information necessary to evaluate welding induced phase transformations under real welding conditions.
2. A three dimensional heat transfer and fluid flow model was used to predict the thermal gradients around the weld, and this information was further used to develop and apply a numerical model based on a modified Johnson–Mehl–Avrami analysis that takes into account non-uniform weld heating and transformation in the $\alpha + \gamma$ two-phase field for the determination of the kinetics of the ferrite to austenite transformation during weld heating. Using the SRXRD experimental data and an activation energy $Q=117.1$ kJ/mole, the JMA kinetic parameters for the $\alpha \rightarrow \gamma$ phase transformation were determined to be $\ln(k_0)=12.2$, and $n=1.45$. These kinetic parameters are consistent for a phase transformation controlled by diffusion of carbon with zero nucleation rate.
3. TTT and CHT diagrams were calculated for the 1005 steel using the kinetic data determined from the SRXRD experiments, providing a graphical means to predict the ferrite to austen-

ite transformation on weld heating for the 1005 steel used in this investigation. These diagrams show that a significant level of superheat is required for the initiation and completion of the phase transformation under the heating rates common to arc welding.

The $\alpha \rightarrow \gamma$ transformation represents only the first step in the evolution of the weld HAZ microstructure. After the complete transformation of the microstructure to γ , continued heating will result in significant grain growth. Since grain size influences the transformation kinetics, it is necessary, in the future, to incorporate a suitable grain growth model into the numerical weld modeling code to predict the austenite grain size distribution. Based on this knowledge, a transformation model, such as that developed by Bhadeshia et al. [33], can be incorporated into a comprehensive weld model and used to calculate CCT diagrams for this alloy. Such a model will ultimately allow for the prediction of HAZ microstructural evolution under a wide range of welding conditions.

Acknowledgements

This work was performed under the auspices of the US Department of Energy, Lawrence Livermore National Laboratory, under Contract No. W-7405-ENG-48. We also acknowledge a grant, DE-FGO2-01ER45900, from the US Department of Energy, Office of Basic Energy Sciences, Division of Materials Sciences to The Pennsylvania State University. Portions of this research were carried out at the Stanford Synchrotron Radiation Laboratory, a national user facility operated by Stanford University on behalf of the US Department of Energy, Office of Basic Energy Sciences. The authors would like to express their gratitude to Dr. Joe Wong of LLNL for assisting with the synchrotron experiments, and Dr. Suresh Babu for assisting with the data analysis and performing Thermocalc calculations. Finally, we wish to also express our gratitude to Mr. Robert Kershaw of LLNL, who sadly passed away this year. Bob Kershaw performed the optical metallography shown in this paper as well as all our other papers on this subject. His

outstanding metallographic expertise will be missed by all of us who have worked with him over the years.

Appendix A. SRXRD data conversion to volume fraction austenite

In the conversion of the integrated intensities of the SRXRD diffraction peaks to volume fractions of austenite and ferrite, there are several effects which must be taken into account. For example, the crystal structure and temperature are two factors which affect the integrated intensity of each observed diffraction peak. These factors and others are discussed in more detail in standard X-ray diffraction references [36]. The general methodology used to convert the raw integrated intensities into the volume fraction of each phase is given below. Where material parameters are required, the corresponding data for iron are used, since the AISI 1005 C-Mn steel contains more than 99 wt. pct. iron.

The structure factor (F) enters into any scattering intensity calculation and increases the measured peak intensity. This factor depends on the incident wavelength, the Bragg angle of the peak, and the atomic scattering factor and crystal structure of the X-ray target. The amplitude of the scattered beam scales linearly with the amplitude of the complex structure factor, so the intensity of the resultant peak scales with its square. For bcc and fcc crystal structures, the squares of the structure factor magnitudes are given by:

$$|F|^2 = (4f)^2 \text{ (bcc)} \quad (\text{A1})$$

$$|F|^2 = (2f)^2 \text{ (fcc)} \quad (\text{A2})$$

where f is the atomic scattering factor, estimated by interpolation of a polynomial fit to tabulated data for iron.

A factor accounting for the possibility of multiple permutations of the Miller indices contributing to a single reflection, thereby increasing the measured intensity is considered next. The multiplicity factor, p , is defined as the number of permutations of position and sign of $\pm h$, $\pm k$, $\pm l$ for planes with the same interplanar spacing and structure factor amplitude.

The systematic broadening of the peaks due to various geometrical considerations is next taken into account. Three such considerations make up the Lorentz factor: (1) a broadening and attenuation of all peaks due to the near-Bragg angle scattering, which scales to the theoretical peak intensities by a factor of $(\sin 2\theta)^{-1}$, (2) the number of planes oriented at or around the Bragg angle is proportional to $\cos\theta$ and (3) the angular dependence of the energy density of the diffracted peaks, which affects the scattered intensity by a factor of $(\sin 2\theta)^{-1}$.

$$\begin{aligned} \text{Lorentz factor} &= \left(\frac{1}{\sin 2\theta}\right)(\cos\theta)\left(\frac{1}{\sin 2\theta}\right) \quad (\text{A3}) \\ &= \frac{1}{4\sin^2\theta\cos\theta} \end{aligned}$$

Combining this relationship with the polarization dependence from the Thompson scattering formula and neglecting a constant factor of 1/8, we obtain the Lorentz–polarization factor:

$$\text{Lorentz–polarization factor} = \frac{1 + \cos^2 2\theta}{\sin^2\theta\cos\theta} \quad (\text{A4})$$

Since the heat-affected zone is in a temperature gradient, it is further necessary to incorporate a temperature factor describing the attenuation of atomic scattering factors due to thermal vibrations:

$$\text{Temperature factor} = e^{-2M} \quad (\text{A5})$$

In practice, the dimensionless quantity M is difficult to calculate. However, the Debye approximation, which is valid for pure elements possessing a cubic crystal structure, is used here. The cubic lattice is approximated as an isotropic continuum in which the vibration wave velocity is uniform, calculated as an average of the velocities of the transverse and longitudinal modes [35]. This approximation is quite good for temperatures above the Debye characteristic temperature, and since the first allotropic transition upon heating in Fe ($\alpha \rightarrow \alpha + \gamma$) occurs at 720 °C (993 K) and the Debye temperature of Fe is 430 K, its use here is easily justified. Debye’s treatment gives the following result:

$$M \approx \frac{6h^2T}{mk\Theta^2} \left[\phi(x) + \frac{x}{4} \right] \left(\frac{\sin\theta}{\lambda} \right)^2 \quad (\text{A6})$$

where h is Planck’s constant, T is the absolute temperature, m is the mass of the vibrating atom (9.273×10^{-26} kg for Fe), k is Boltzmann’s constant, Θ is the Debye characteristic temperature of the substance in kelvins (430 K for Fe), $x \equiv \Theta/T$, and where

$$\phi(x) \equiv \frac{1}{x} \int_0^x \frac{\xi}{e^\xi - 1} d\xi \quad (\text{A7})$$

The relative intensity of each peak is given by the following relation:

$$I = I_0/R \quad (\text{A8})$$

where I_0 is the integrated area of the peak and the scaling factor, R , which includes the structure factor, the multiplicity, the Lorentz–polarization factor, and the temperature factor:

$$R = |F|^2 p \left(\frac{1 + \cos^2 2\theta}{\sin^2\theta\cos\theta} \right) e^{-2M} \quad (\text{A9})$$

The austenite and ferrite volume fractions are calculated by dividing the sum of the phase-fraction scaled peak intensities for a given phase by the total of all phase-fraction scaled peak intensities in each diffraction pattern.

Appendix B. Non-isothermal Johnson–Mehl–Avrami equation applicable to two-phase equilibrium

In Eq. (3), the extent of the transformation $f_e(t)$ is related to the volume fraction of product phase by the following equation:

$$f_e(t) = \frac{f(t)}{F} \quad (\text{B1})$$

where $f(t)$ is the volume fraction of product phase after time t , and F is the equilibrium fraction of the product phase at temperature T . For transformations of the eutectoid type, i.e. the transformation path involves one phase transforming directly to another at a constant temperature. In these types of transformations $f_e(t)$ is identical to $f(t)$ since F is equal to 1. In many instances, such as the α -ferrite to austenite transformation during heating of low carbon steels, the transformation path involves

$\alpha \rightarrow (\alpha + \gamma) \rightarrow \gamma$. In the $\alpha + \gamma$ two-phase region, F is not equal to 1 and can be calculated from the corresponding phase diagram. Substituting Eqs. (4) and (B1) into Eq. (3), the isothermal JMA equation is rewritten as:

$$\frac{f(t)}{F} = 1 - \exp\left[-\left\{k_0 \times \exp\left(-\frac{Q}{RT}\right) \times t\right\}^n\right] \quad (\text{B2})$$

For eutectoid-type reactions, i.e. $F = 1$, the non-isothermal solution of the JMA equation has been derived by Krüger [36]. However, Krüger's formulation does not apply to systems where the transformation involves a two-phase region. Here, the JMA equation is extended to deal with such a two-phase region under non-isothermal conditions. In the following derivation, to simplify the problem, we assume that the kinetic parameters Q , k_0 , and n are independent of temperature, i.e. there is no significant change in the nucleation and growth mechanisms during the phase transformation [32].

During a non-isothermal solid-state transformation, the temperature changes continuously with the time, i.e. $T = T(t)$. In the following discussion, the non-isothermal kinetic equation will be derived under continuous heating conditions. The derivation procedure and the resulting equation are the same for continuous cooling conditions. The continuous change of the temperature with time can be approximated by subsequent isothermal steps of the duration Δt . The temperature–time curve starts at time $t_0 = 0$ and temperature T_1 , and finishes at time $t_m = m\Delta t$ and temperature T_{m+1} . It should be noted that time equal to 0 is defined from the instant the sample reaches the isothermal transformation temperature. This continuous curve is discretized into m isothermal steps. For example, the temperature between times t_{i-1} and t_i is equal to T_i , and at the time t_i , the temperature is changed from T_i to T_{i+1} . This temperature (T_{i+1}) prevails between times t_i and t_{i+1} .

The γ fraction converted along the i th isothermal time step ($t_{i-1} \leq t \leq t_i$) is expressed as:

$$\frac{f(t)}{F_i} = 1 - \exp\left\{-\left[k_0 \times \exp\left(-\frac{Q}{RT_i}\right) \times (t - c_i)\right]^n\right\} \quad (\text{B3})$$

where T_i is the temperature at the i th step, F_i is the

equilibrium fraction of the new phase at temperature T_i , and c_i is a time used to account for the pre-converted fraction of new phase at the beginning of i th step. The term c_i ($c_1 = 0$) is determined from the continuity relation that the fraction calculated using Eq. (B3) at the beginning of the i th time step is equal to that converted at the end of $(i-1)$ th time step, $f(t_{i-1})$. Substituting $t = t_{i-1} = (i-1)\Delta t$ into Eq. (B3), we have:

$$c_i = (i-1)\Delta t - \frac{n \sqrt{-\ln\left[1 - \frac{f(t_{i-1})}{F_i}\right]}}{k_0 \times \exp\left(-\frac{Q}{RT_i}\right)} \quad (\text{B4})$$

where Δt is the time step.

We can define the second term in Eq. (B4) as another time constant τ_i ($\tau_1 = 0$).

$$\tau_i = \frac{n \sqrt{-\ln\left[1 - \frac{f(t_{i-1})}{F_i}\right]}}{k_0 \times \exp\left(-\frac{Q}{RT_i}\right)} \quad (\text{B5})$$

Thus, we can obtain the fraction of new phase converted at the end of i th step by substituting $t = t_i = i\Delta t$ and $c_i = (i-1)\Delta t - \tau_i$ into Eq. (B3).

$$\frac{f(t_i)}{F_i} = 1 - \exp\left\{-\left[k_0 \times \exp\left(-\frac{Q}{RT_i}\right) \times (\Delta t + \tau_i)\right]^n\right\} \quad (1 \leq i \leq m) \quad (\text{B6})$$

Eq. (B6) is the non-isothermal kinetic equation considering the equilibrium fraction of new phase in two-phase region. Further details of the derivation of Eq. (B6) are available elsewhere [37].

References

- [1] Honeycomb RWK, Bhadeshia HKDH. Steels, microstructure and properties. Metals Park (OH): American Society of Metals, 1982.
- [2] Jones S, Bhadeshia HKDH. Metall Mater Trans A 1997;28A(10):2005.
- [3] Bhadeshia HKDH. Bainite in steels. 2nd ed. London: Institute of Materials, 2001.
- [4] Krauss GS. Steels: Heat treatment and processing principles. Materials Park (OH): ASM International, 1990.

- [5] Vander Voort GF. Atlas of time-temperature diagrams for irons and steels. Materials Park (OH): ASM International, 1991.
- [6] Harrison PL, Farrar RA. *Int Mat Rev* 1989;34(1):35.
- [7] Grong Ø. Metallurgical modelling of welding. London: The Institute of Materials, 1994.
- [8] Easterling K. Introduction to the physical metallurgy of welding. London: Butterworths and Co, 1983.
- [9] Ashby MF, Easterling KE. *Acta Metall* 1982;30:1969.
- [10] Ion JC, Easterling KE, Ashby MF. *Acta Metall* 1984;32:1949.
- [11] Elmer JW, Wong J, Ressler T. *Metall Mater Trans A* 2001;32A(5):1175.
- [12] Zhang W, Elmer JW, DebRoy T. *Scripta Mater* 2002;46:753.
- [13] Zhang W, Elmer JW, DebRoy T. *Mater Sci Eng A* 2002;333(1-2):320.
- [14] Mundra K, DebRoy T, Kelkar K. *Numer Heat Trans* 1996;29:115.
- [15] Mundra K, Blackburn JM, DebRoy T. *Sci Technol Welding Joining* 1997;2(4):174.
- [16] Yang Z, DebRoy T. *Metall Mater Trans B* 1999;30B:483.
- [17] Pitscheneder W, DebRoy T, Mundra K, Ebner R. *Welding J* 1996;75:71s.
- [18] Karpenko V, Kinney JH, Kulkarni S, Neufeld K, Poppe C, Tirsell KG, Wong J, Cerino J, Troxel T, Yang J, Hoyer E, Green M, Humpries D, Marks S, Plate D. *Rev Sci Instrum* 1989;60:1451.
- [19] Elmer JW, Wong J, Fröba M, Waide PA, Larson EM. *Metall Mater Trans A* 1996;27A(3):775.
- [20] Elmer JW, Wong J, Ressler T. *Metall. Mater Trans A* 1998;29A(11):2761.
- [21] Ressler T, Wong J, Elmer JW. *J Phys Chem B* 1998;102(52):10724.
- [22] Wong J, Fröba M, Elmer JW, Waide PA. *J Mat Sc* 1997;32:1493.
- [23] Bearden JA, Burr AF. *Rev Mod Physics* 1967;39:125.
- [24] Palmer TA, Elmer JW, Wong J. *Sci Tech Weld Join* 2002;7(3):159.
- [25] Babu SS. Private communications, Oak Ridge National Laboratory, 2000.
- [26] Sundman B, Jansson B, Andersson J. *Calphad-Computer Coupling of Phase Diagrams and Thermochemistry* 1985;9(2):153.
- [27] Patankar SV. Numerical heat transfer and fluid flow. Hemisphere Pub Corp, 1980.
- [28] Samuels LE. Optical microscopy of carbon steels. Materials Park (OH): American Society for Metals, 1980 p.69.
- [29] Speich GR, Demarest VA, Miller RL. *Metall Trans A* 1981;12:1419.
- [30] Nath SK, Ray S, Mathur VNS. *ISIJ Inter* 1994;34:191.
- [31] Askill J. Tracer diffusion data for metals, alloys and simple oxides. IFI/Plenum Press, 1970.
- [32] Christian JW. The theory of transformations in metals and alloys, Part I. 2nd ed. Oxford: Pergamon, 1975.
- [33] Bhadeshia HKDH, Svensson LE. Modelling the evolution of microstructure in steel weld metal. In: Easterling KE, Cerjak H, editors. Mathematical modeling of weld phenomena. London: Institute of Materials; 1993. p. 109.
- [34] Cullity BD, Stock SR. Elements of X-ray diffraction. 3rd ed. Upper Saddle River (NJ): Prentice Hall, 2001.
- [35] James RW. The optical principles of the diffraction of X-rays. Woodbridge (CT): Ox-Bow Press, 1982.
- [36] Kruger PJ. *Phys Chem Solids* 1993;54:1549.
- [37] Zhang W, Elmer JW, DebRoy T. Modeling of Ferrite to Austenite Transformation and Real Time Mapping of Phases during GTA Welding of 1005 Steel, accepted for publication in Trends in welding Research, Materials Park, (OH), ASM International, 2002.